A Zero-Field Single-Molecule Magnet with Luminescence Thermometry Capabilities Containing Soft Donors

Riccardo Marin,[a]*† Diogo Alves Gálico,[b]† Rezeda Gayfullina,[c] Jani O. Moilanen,[c] Luís D. Carlos,[d] Daniel Jaque,[a,e] and Muralee Murugesu[b]*

Simultaneous fine-tune of magnetic and optical properties in lanthanide single-molecule magnets (SMMs) is a daunting task. Even more so when additional functionalities, like luminescence thermometry, are sought after. Herein, we explore the use of a ligand with both soft and hard donor atoms (thiobenzoate, tba^-) as a strategy to prepare a multifunctional optomagnetic lanthanide complex. The proposed mononuclear Dy^{3+} complex acts as a zero-field SMM, whose energy barrier to magnetization reversal was confirmed from the analysis of the photoluminescence spectrum. Moreover, the temperature dependence of the emission spectral profile was harnessed to build a thermometric approach working below 12 K – where the complex behaves as an SMM. In search for general trends informing the preparation of similar multifunctional SMMs, we modelled the electronic properties of a series of complexes where the sulfur atom of tba^- is replaced for other chalcogens (O, Se, Te). These calculations show that careful choice of ligands with soft donor atoms can boost both magnetic and thermometric performances, paving the way for the rational design of novel multifunctional lanthanide complexes.

Introduction

In the fast-paced digital era, information is created and exchanged at an unprecedented rate, thus requiring increasingly efficient physical storage units. In addition, electronic devices are undergoing extreme miniaturization and the first case of "quantum supremacy"–i.e., a quantum processor outperforming a classical computer–was recently reported.[1] In the frame of this digital revolution, single-molecule magnets (SMMs) are prime candidates for becoming building blocks of the next-generation of electronic devices. Lanthanide (Ln^{3+}) complexes are the cream of the crop of this family of compounds,[2-4] with working temperatures recently reaching the boiling point of liquid nitrogen–bringing these species one step closer to real-world applications.[5]

To ensure the proper functioning of an SMM, its temperature should be controlled and maintained below a specific threshold. To that end, we reported the first examples of Ln^{3+}-SMMs whose photoluminescence (PL) can be harnessed to monitor their thermal state.[6-11] However, the preparation of Ln^{3+}-complexes simultaneously performing well as SMMs and luminescent thermometers is no easy task, and it requires judicious choice of the ligand framework, metal, and coordination geometry .[8, 12] In this context, ligands containing soft donors like heavy chalcogens (E = S, Se, Te) hold promise. This is because the large radial extension of their valence orbitals affects the ligand field around the metal centre. Ln-E bonds have also lower associated vibrational energies compared to Ln-O bonds. Not only this promotes high barrier to magnetization reversal (U_{eff})[13, 14], but also supports efficient Ln^{3+} PL.[15] Yet, these ligands are underexplored compared to N- and O-containing ligands

Moving from these considerations, we propose the first example of soft-donor-containing SMM acting as luminescent thermometer in the form of a novel thiobenzoate (tba^-)-based Dy^{3+} complex: $[Dy(tba)_3phen]\cdot CH_2Cl_2$ (**1**; phen = 1,10-phenanthroline). This complex brings together the stable Ln-O interaction along with the property-modulating features imparted by Ln-S bonds. Analysis of the photoluminescence (PL) spectrum allowed interpreting the magnetic relaxation mechanism of this zero-field SMM, while the temperature-dependent spectral variations were harnessed to develop a luminescence thermometric approach. Stimulated by these results, we deepened our exploration of soft-donor-containing ligands for tuning optical and magnetic features in complexes with the use of *ab initio* and density functional theory calculations. Modelling of a series of Dy^{3+} complexes generated from **1** replacing tba^- for benzoate, selenobenzoate, and tellurobenzoate show trends of optical and magnetic properties that highlight how soft donor atoms can be valuable allies in pursuit of luminescent SMMs with thermometric capabilities.

Results and Discussion

[a] *Nanomaterials for Bioimaging Group (nanoBIG), Departamento de Física de Materiales, Facultad de Ciencias, Universidad Autónoma de Madrid, C/ Francisco Tomás y Valiente 7, Madrid 28049, Spain. E-mail: riccardo.marin@uam.es*

[b] *Department of Chemistry and Biomolecular Sciences, University of Ottawa, Ottawa, Ontario K1N 6N5, Canada. E-mail: m.murugesu@uottawa.ca*

[c] *Department of Chemistry, University of Jyväskylä, Jyväskylä, FI-40014, Finland.*

[d] *Phantom-g, CICECO – Aveiro Institute of Materials, Department of Physics, Universidade de Aveiro, 3810-193, Aveiro, Portugal.*

[e] *Nanomaterials for Bioimaging Group (nanoBIG), Instituto Ramón y Cajal de Investigación Sanitaria, Hospital Ramón y Cajal, Ctra. De Colmenar Viejo, Km. 9100, 28034, Madrid, Spain.*

Electronic Supplementary Information (ESI) available: experimental details, structural and chemical characterization, additional magnetic data, mathematical treatment of luminescence thermometry, computational details and simulation of the thermometric performance. See DOI: 10.1039/x0xx00000x

Structural characterization.

$[Dy(tba)_3phen]\cdot CH_2Cl_2$ (**1**) was synthesized by adding an aqueous solution of $Dy(NO_3)_3\cdot 5H_2O$ to a solution of potassium thiobenzoate (Ktba) and phen in water (Ktba:phen = 3:1). The precipitated yellow powder was recrystallized from dichloromethane (DCM), yielding transparent, pale yellow crystals with needle-like morphology. Details about the experimental procedure are given in the ESI. Complex **1** crystallizes in the monoclinic $P2_1/c$ space group, with three DCM crystallization molecules for every four complex molecules in the structure (**Figure 1**, **S1** and **Table S1**).

These DCM molecules evaporate from the lattice when the crystals are exposed to the atmosphere for a prolonged time, resulting in loss of crystallinity. The octa-coordinated Dy^{3+} ion adopts a distorted triangular dodecahedron configuration (D_{2d} maximum symmetry – see Table S2) observed in other mononuclear and dinuclear Dy^{3+} SMMs.[16, 17] The coordination environment of Dy^{3+} is composed of three oxygen and three sulphur atoms belonging to the tba^- ligands, along with two phen nitrogen atoms. The Dy···O distances range between 2.34 and 2.37 Å, while Dy···S bonds are longer (2.80-2.84 Å). These values are in line with other lanthanide coordination compounds based on tba^-.[18, 19] Inspection of the packing (**Figure S2**) reveals a 3D arrangement of the complexes governed by π-π stacking (**Figure S3**) both in the face-to-face and edge-to-face configurations–centroid-to-centroid distances of 3.76 and 4.78 Å, respectively (see ESI for more details). Within the crystal, the shortest intermolecular Dy···Dy distance is 7.20 Å (**Figure S3**).

We should point out that in Ln^{3+}-complexes Ln-E bonds are less common than Ln-O ones, owing to the weaker interaction between Ln^{3+} (hard acid) and E (soft donor). Among E-containing ligands, carbamates, xanthates, and diphenyl chalcogenides are the most studied ones.[20-23] Thiobenzoate has instead been poorly investigated, with only two reported Ln^{3+}-tba complexes to date.[18, 19] Yet, as observed in **1**, this ligand can promote both magnetic and PL properties in Ln^{3+}-complexes, since it provides simultaneously strong and stable Ln-O interaction along with property modulation imparted by Ln-S bonds.

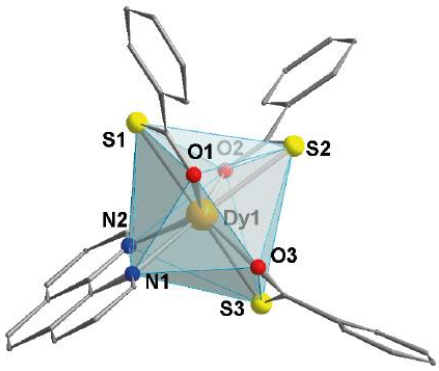

Figure 1. Partially labelled molecular structure of (**1**). Hydrogen atoms are omitted for clarity. Colour code: Dy – orange; O – red; S – yellow; N – blue.

Magnetic characterization.

To investigate the magnetic properties of **1**, the dc (direct current) magnetic susceptibility was first measured between 300-1.8 K under an applied field of 1000 Oe (**Figure S5A**). The χT product exhibited a gradual decrease from 14.15 to 12.41 cm^3 K mol^{-1} upon cooling from 300 to 1.8 K. Its value at room temperature is in good agreement with the theoretical value for a single Dy^{3+} ion (S = 5/2, L = 5, $^6H_{15/2}$ g = 4/3, C = 14.17 cm^3 K mol^{-1}). The decrease at low temperature can arise from a combination of thermal depopulation of Stark sublevels, significant magnetic anisotropy, and small yet non-negligible antiferromagnetic intermolecular interactions between Dy^{3+} centres.[12] The presence of magnetic anisotropy was confirmed by the field-dependent magnetization observed in the magnetization (M *vs.* H) and reduced magnetization (M *vs.* HT^{-1}) plots, which reaches a maximum value of 5.70 $M\mu_B$ at 1.9 K and 7 T (**Figure S5b**). Therein, the non superimposition of the isofield lines indicates the presence of non negligible magnetic anisotropy (**Figure S5c**).

The SMM properties of **1** were studied via ac (alternating current) susceptibility measurements in the 0.1-1500 Hz range with an oscillating field H_{ac} = 3.78 Oe. Below 12 K, frequency-dependent susceptibility was observed (**Figure 2a**) indicative of slow relaxation of the magnetization intrinsic to the molecule. In the absence of an external field (H_{dc} = 0 Oe), a frequency-dependent signal was observed with a strong contribution of quantum tunnelling of magnetization (QTM) at low temperature. QTM within the ground KD is not fully suppressed despite the good axiality of the **g**-tensor of the ground KD ($\mathbf{g}_x$ = $\mathbf{g}_y$ = 0.001 and $\mathbf{g}_z$ = 19.832; *vide infra*). This observation is supported by the calculated transition magnetic moment matrix elements between the spin-orbit states in the ground multiplet of $^6H_{15/2}$ (*vide infra*). To probe the mechanisms responsible for the spin-reversal, the relaxation times (τ) of the individual peaks were extracted from the χ'' data using the generalized Debye model (**Table S3-S5**).[24] Considering the most common relaxation mechanisms – Orbach, Raman, and QTM – and the temperature regimes at which they operate, the τ^{-1} *vs.* T dataset (**Figure 2c, S6a**) was fit to the following equation:

$$\tau^{-1} = \tau_0^{-1}\exp\left[-U_{eff}/K_bT\right] + CT^n + B_1/(1 + B_2H^2) \quad (1)$$

The best-fit values (**Table S6**) indicate that **1** acts as a zero-field SMM with thermally activated relaxation *via* the Orbach mechanism (U_{eff} = 136.8 K, 95.1 cm^{-1}). Spectroscopic analysis supports the attribution of this relaxation through the first excited *mj* level, similarly to what indicated by calculations (*vide infra*).

To determine the optimal applied dc field that minimizes QTM at low temperature, field-dependent relaxation dynamics were investigated at 5 K (**Figure S7**). Frequency-dependent signals in the out-of-phase χ'' susceptibility were observed between 0 and 5000 Oe. The field-dependent τ values were obtained fitting the χ'' susceptibility to the generalized Debye model, and the resulting τ^{-1} *vs.* T dataset was fit with the following equation

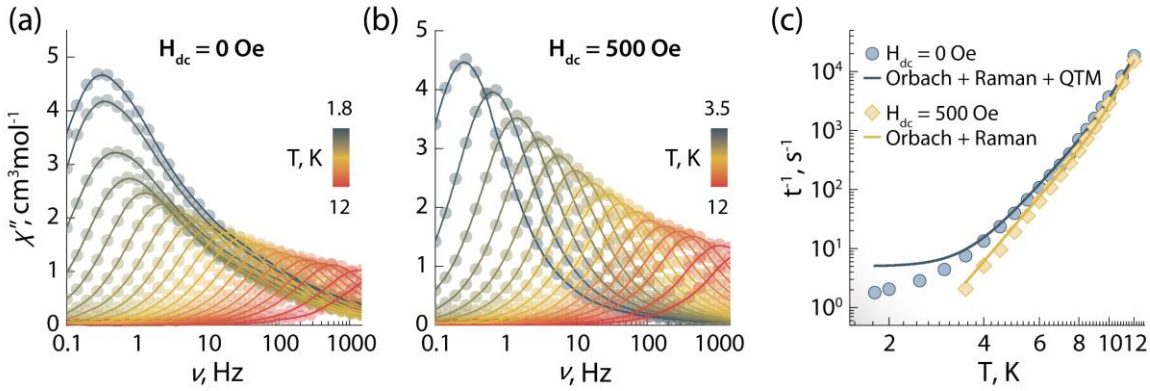

Figure 2. Frequency dependence of the out-of-phase (χ'') magnetic susceptibility as a function of temperature obtained in absence of an external dc magnetic field (**a**) and under an applied static field of 500 Oe (**b**). **c)** Temperature dependence of the magnetic relaxation times (τ) in absence (blue circles) and in the presence of a 500 Oe applied field (yellow diamonds). Solid lines are the best fit to the experimental data using Eq. (1).

(which includes the field-dependent direct, Raman, and QTM mechanisms):

$$\tau^{-1} = AH^4 + CT^n + B_1/(1 + B_2H^2) \qquad (2)$$

Introduction of the Orbach (field-independent) term did not lead to a better fit and was hence excluded to avoid overparametrization. The best-fit values (**Table S7**) indicates that the relaxation dynamics when $H_{dc} \leq 450$ Oe are governed by QTM, and for $H_{dc} \geq 1800$ Oe the direct mechanism becomes dominant. Hence, an optimal field of 500 Oe was chosen to ensure minimal contributions from both mechanisms. Indeed, temperature-dependent ac studies under an external field of 500 Oe (**Figure 2b**) confirmed the complete suppression of the QTM mechanism (**Figure 2c, S6b**). Even after QTM suppression, magnetic relaxation continues to occur via the first excited mj level (138.2 K, 96.1 cm^{-1}). Magnetic hysteresis measurements revealed no retention of the magnetic moment at 1.8 K.

Optical properties and luminescence thermometry.

The combination of ligands and Dy^{3+} in **1** yields also augmented optical properties, with the emission spectrum being dominated by the typical Ln^{3+} narrow emission lines (**Figure 3a**). The excitation spectrum recorded monitoring the Dy^{3+} emission at 570 nm shows the presence of both sharp and broadband features (**Figure 3a**), ascribed respectively to the 4f-4f Ln^{3+} transitions and the organic ligands. The appearance of this latter contribution is indicative of ligand-sensitized emission. In this process, the ligands absorb the excitation photons and transfer the optical energy to the coordinated metal centre, which then relaxes radiatively to its ground state (i.e., emits photons). Upon fitting with a single exponential function the decay curve obtained monitoring the Dy^{3+}: $^4F_{9/2} \rightarrow {}^6H_{13/2}$ transition (**Figure 3b**), a characteristic decay time of 40 μs was found for the Dy^{3+} emitting state ($^4F_{9/2}$). This value is almost 3 times larger than the lifetime of the luminescent Dy^{3+}-SMM with thermometric capabilities we recently reported,[6] and similar to the value observed in a dimetallic ZnDy SMM.[4]

The $^4F_{9/2} \rightarrow {}^6H_{15/2}$ transition was deconvoluted (**Figure 3c**) to garner information regarding the mj levels of the ground level ($^6H_{15/2}$), obtaining an energy separation of 92 cm^{-1} between the first two mj levels–in agreement with the calculated value of 107 cm^{-1} (*vide infra*) and larger or on par than other optomagnetic Dy^{3+} complexes.[4, 6, 25] This value is close to the energy barriers observed in ac magnetic studies (95.1 and 96.1 cm^{-1}, without and with applied field, respectively), and hence indicates that the Orbach magnetic relaxation process occurs through the first excited mj level.

The PL of the systems shows also sensitivity towards temperature changes, and can thus be employed for thermal monitoring purposes.[12] To study the thermometric performance of **1**, we recorded PL spectra between 10 and 50 K (**Figure 4a**). This range encompasses the high end of the temperature window wherein **1** acts as SMM – i.e., <12 K. Variations in the relative intensities of the Stark components of the $^4F_{9/2} \rightarrow {}^6H_{13/2}$ manifold were observed.

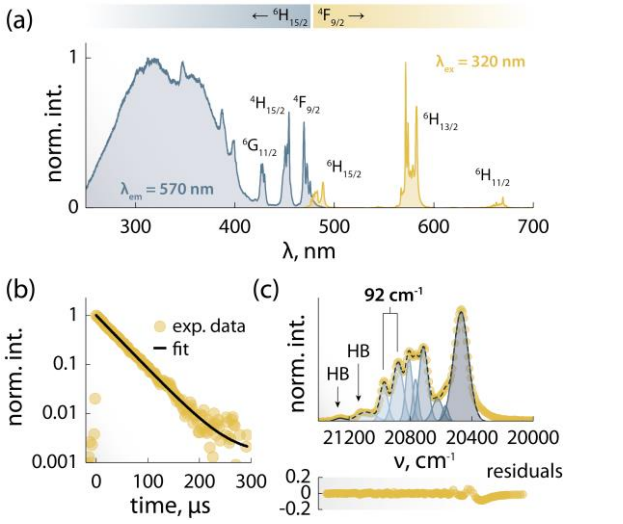

Figure 3. Spectroscopic studies of **1**. **a)** Excitation (blue) and emission (yellow) spectra recorded respectively with λ_{em} = 570 nm and λ_{ex} = 320 nm at 10 K. The main Dy^{3+} transitions are labelled. **b)** Decay curve recorded at 10 K monitoring the emission at 570 nm ($^4F_{9/2} \rightarrow {}^6H_{13/2}$) under 320-nm excitation (yellow circles) and its fit to a single-exponential decay (black line). **c)** Top: Zoom-in of the $^4F_{9/2} \rightarrow {}^6H_{15/2}$ transition (yellow circles) and its fit (dark blue sdashed line) obtained from the sum of Gaussian peaks (blue solid lines). Bottom: Residuals ($R^2 \approx 0.99$). The retrieved position of the first two $^6H_{15/2}$ *mj* levels is indicated with vertical lines, along with their energy separation. HB = hot band.

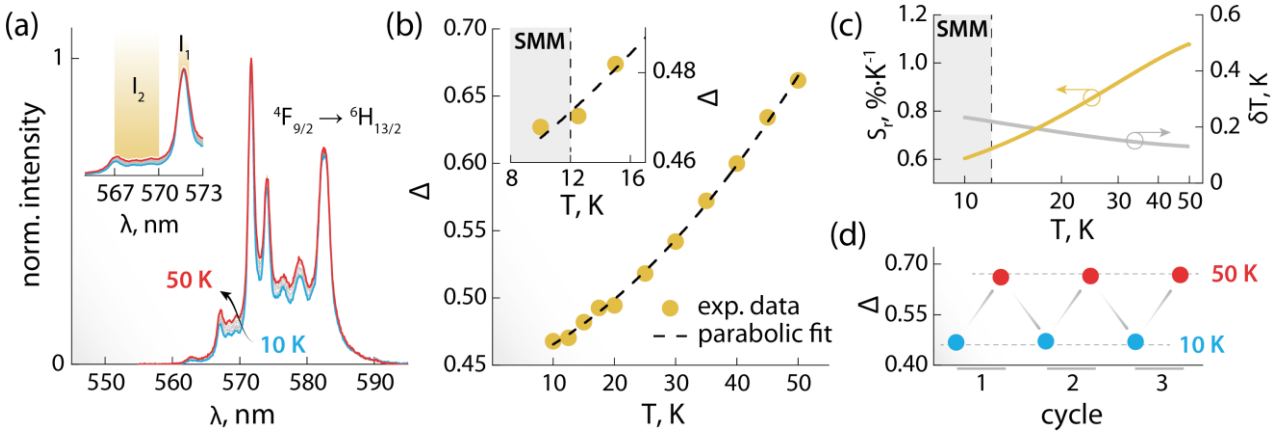

Figure 4. Luminescence thermometry performance of **1**. **a)** PL spectra recorded in the 10-50 K range under 320 nm excitation. In the inset, a zoom-in of the 565-573 nm range is shown, along with the integration ranges I_1 and I_2 (yellow) used for calculating the areas used to obtain the thermometric parameter (Δ). **b)** Calibration curve obtained using the thermometric parameter $\Delta = I_2/I_1$ (yellow circles) and its fit to a parabolic function (dashed black line). In the inset, a zoom-in of the 8-17 K range is shown. The range wherein **1** behaves as SMM is indicated as a grey rectangle. **c)** Relative thermal sensitivity and associated uncertainty calculated from the data in **(b)** and the mathematical treatment detailed in the Supporting Information. A logarithmic scale is used for the abscissa to better visualize the low-temperature range. **d)** Results of three cycles of measurements performed at 10 and 50 K to determine the repeatability of the thermometric approach.

The ratio between the intensity integrated over conveniently selected ranges (I_1 and I_2, as indicated in the inset of **Figure 4a**) was chosen as thermometric parameter ($\Delta = I_2/I_1$, **Figure 4b**). The Δ vs. T dataset was fit to a parabolic function (**Table S8**) that, along with its first derivative, was used to determine the relative thermal sensitivity according to the following equation:[26, 27]

$$S_r = \frac{1}{\Delta}\frac{\partial \Delta}{\partial T} \qquad (3)$$

The obtained relative thermal sensitivity varies between 0.6 and 1.1 %·K^{-1} over the 10-50 K range (**Figure 4c**): a performance on par with other thermometers based on spectral variations within the same manifold[7, 9, 28] and other Ln^{3+}-coordination compounds working in this low-temperature range.[29, 30] The uncertainty associated with the thermal reading varies between 0.1 and 0.2 K, while the repeatability of the thermometric approach is 98.9% (**Figure 4d, Table S9**). The obtained uncertainty is in line with typical values found for measurements performed with photomultipliers.[27] Details about the mathematical treatment of the data are given in the ESI. Notably, within the temperature range where the complex behaves as SMM, the thermometric approach holds (grey rectangles in **Figure 4b** and **4c**). This observation opens the door to the thermal monitoring of **1** via PL during its operation as SMM. If overheating is optically detected, corrective actions could be taken to avoid failure (e.g., operation interruption or further cooling). Although the relative thermal sensitivity of this complex is lower than the one of the other reported zero-field SMM (based on Ho^{3+}),[31] the data treatment required here is much less laborious. Indeed, a careful background subtraction–necessary to isolate 4*f*-4*f* reabsorption features from the ligand emission–is not required. This aspect makes the proposed system/approach more straightforwardly implementable in real-life applications.

Theoretical modelling of the chalcogen atom effects.

Stimulated by the experimental results, we decided to model the effect of hard (O) and soft (S, Se, and Te) donor atoms on the magnetic and optical properties of the reported optomagnetic complex (**Tables S10-S24**). Specifically, we were interested in the general trends that could serve as a predictive tool to fine-tune simultaneously the magnetic, optical, and thermometric performance of a Ln^{3+}-SMM. With this goal in mind, density functional theory (DFT) and CASSCF/RASSI calculations were thus performed on systems $\mathbf{1_O}$, $\mathbf{1_S}$, $\mathbf{1_{Se}}$, and $\mathbf{1_{Te}}$, containing benzoate (ba^-), thiobenzoate (tba^-), selenobenzoate (sba^-), and tellurobenzoate ($teba^-$), respectively (**Figure 5**). The results show that in $\mathbf{1_O}$, the stabilization and axiality of the ground Kramers doublet (KD; **Table S13**) are lost. Hence, a low U_{eff} (32 cm^{-1}) and significant QTM within the ground KD are observed. However, the microscopic magnetic properties and

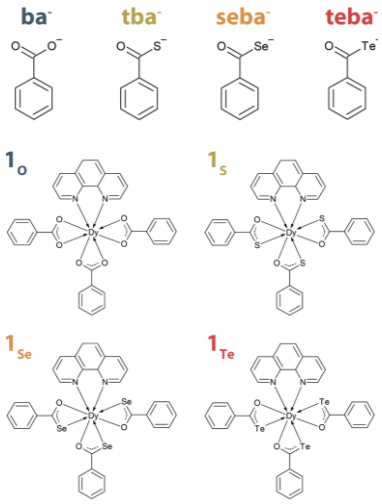

Figure 5. Benzoate, thiobenzoate, selenobenzoate, and tellurobenzoate ligands, along with the corresponding complexes derived from **1**.

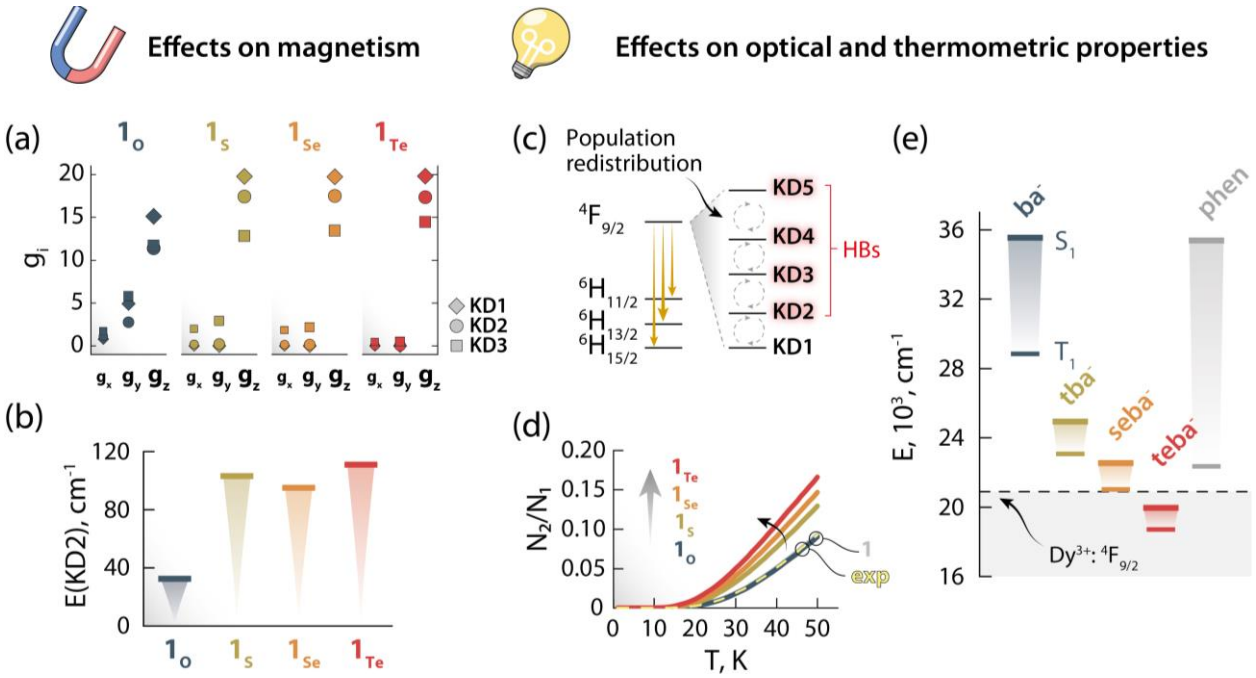

Figure 6. The effects of changing the chalcogen atom in the benzoate ligand on the magnetic and optical properties. Components of the **g**-tensor (g_x, g_y, g_z) of the first three KDs **(a)** and energy of KD2 **(b)** for the ground Dy^{3+}:$^6H_{15/2}$ state of $\mathbf{1}_O$, $\mathbf{1}_S$, $\mathbf{1}_{Se}$, and $\mathbf{1}_{Te}$. Scheme depicting the temperature-induced electron population redistribution between the KDs (i.e., *mj* levels) of the Dy^{3+}:$^4F_{9/2}$ excited state **(c)**. Ratio between the electron population of KD2 and KD1 as obtained from the Boltzmann model for $\mathbf{1}_O$, $\mathbf{1}_S$, $\mathbf{1}_{Se}$, and $\mathbf{1}_{Te}$ **(d)**. The results of the same calculations for **1** (solid gray line, beneath $\mathbf{1}_O$) and considering the position of the $^4F_{9/2}$ components obtained from the deconvolution (**Figure S11**) of the $^6H_{15/2} \rightarrow {}^4F_{9/2}$ transition in the excitation spectrum (exp, dashed yellow line) are also reported. The overlap between the curves **1** and $\mathbf{1}_O$ is a serendipitous result stemming from the similar energy difference between the first two $^4F_{9/2}$ *mj* levels obtained for these two systems. Energy of the first singlet (S_1) and triplet (T_1) excited states of the different ligands as obtained using the CAM-B3LYP exchange-correlation functional **(e)**. The position of the Dy^{3+}:$^4F_{9/2}$ excited state is also indicated with a dashed black line (centroid of the $^4F_{9/2}$ manifold obtained from the deconvolution of the $^6H_{15/2} \rightarrow {}^4F_{9/2}$ transition in the excitation spectrum – **Figure S10**).

energy spectrum of the $^6H_{15/2}$ ground multiplet drastically change in $\mathbf{1}_S$, $\mathbf{1}_{Se}$, and $\mathbf{1}_{Te}$ compared to $\mathbf{1}_O$. The height of the energy spectrum is increased (**Figure S8**), the ground KD is more stabilized, the axiality of the lowest KDs is improved (as evinced from the calculated **g**-tensors (**Figure 6a**) and crystal field parameters), the main magnetic axes of the lowest KDs are more collinear (**Figure S9**), and the calculated qualitative energy barriers are higher (**Figure 6b**, **Table S13-S16**). Overall, among $\mathbf{1}_S$, $\mathbf{1}_{Se}$, and $\mathbf{1}_{Te}$, the latter has the best parameters by a slight margin: a result of the elongation and decrease in the ionic nature of Ln-E bonds when descending the chalcogen group.* This is shown by the optimized geometries and calculated electron densities ($\rho(r)$), Laplacians ($\nabla^2\rho(r)$), delocalization indices (DI), and effective atomic charges obtained from the quantum theory of atoms in molecules analysis (**Table S23**). Since the longer radical extensions of valence orbitals of heavier chalcogens weaken the equatorial crystal ligand field around Dy^{3+}, O and N atoms of the carbonyl groups and phen ligand, respectively, start to dominate the axial crystal ligand field of Dy^{3+} ion in $\mathbf{1}_S$, $\mathbf{1}_{Se}$, and $\mathbf{1}_{Te}$. The weakening of the equatorial ligand field around Dy^{3+} ion has been proven to improve the axiality and SMM properties of Dy^{3+}-based SMMs in tandem.[5, 32] This is best illustrated by investigating the calculated crystal-field parameters (B_k^q) and visualizing the main magnetic axis of Dy^{3+} ion in the studied systems. For all other systems, except for $\mathbf{1}_O$, the axial crystal-field parameter B_2^0 dominates the crystal ligand field because its value is order of magnitude larger than the values of any other crystal-field parameters, whereas for $\mathbf{1}_O$ the non-axial crystal-field parameters are of the same magnitude or even larger than the axial crystal-field parameters for all values of *k* (**Table S17-21**). Moreover, the visualization of the main magnetic axis of the first three KDs of Dy^{3+} ion reveals that they are almost collinear in all other system expect in $\mathbf{1}_O$ because of the stronger axiality observed in the heavier chalcogen systems (**Figure S9**). These findings are in line with previous studies on Ln^{3+}-based SMMs containing soft donor atoms from the chalcogen groups.[14, 33]

The nature of chalcogen atom influences the optical properties of the complex and its expected luminescence thermometry performance too. In this study, we have harnessed the spectral changes arising from temperature-induced population redistribution between the *mj* levels (i.e., KDs) to define a ratiometric thermometric approach (**Figure 4**). Specifically, the integrated intensity I_2 mainly contains contributions from hot bands (HBs), i.e., transitions from the Dy^{3+}:$^4F_{9/2}$ excited *mj* levels to the Dy^{3+}:$^6H_{13/2}$ state (**Figure 6c**). I_1 has its major contribution stemming from the lowest Dy^{3+}:$^4F_{9/2}$ *mj* level. The population of each level (N_i) as a function of temperature can be modelled with a system of equations based on the Boltzmann function (see ESI for details). Since the intensity ratio is proportional to the electron population, and considering the low temperature range investigated, the ratio between the electron population of the first excited level and ground level (N_2/N_1) can thus approximate the intensity ratio $\Delta = I_2/I_1$ used for the

thermometric approach. This assumption is corroborated by the overlap between the N_2/N_1-vs-temperature curves (**Figure 6d**) for **1** and using the energy values extracted from the deconvolution of the $^6H_{15/2} \rightarrow {}^4F_{9/2}$ transition in the excitation spectrum (**Figure S11**). Because of the effect that different chalcogen atoms have on the Dy^{3+}:$^4F_{9/2}$ *mj* levels separation (**Tables S13-S16**), the N_2/N_1 curve becomes steeper and has an earlier onset following the order $\mathbf{1}_{Te}$>$\mathbf{1}_{Se}$>$\mathbf{1}_{S}$>$\mathbf{1}_{O}$ (**Figure 6d**). These observations indicate that a thermometric approach based on the fine structure of the $^4F_{9/2} \rightarrow {}^6H_{13/2}$ manifold is more sensitive and can extend to lower temperatures using heavier chalcogens.

Thus, it appears that moving downwards along the chalcogen group can be a viable strategy to simultaneously boost the magnetic properties and luminescence thermometry performance of luminescent Ln^{3+}-SMMs. However, there is an additional piece of the puzzle to consider: the lower energy of the first excited singlet (S_1) and triplet (T_1) states of heavy-chalcogen-containing ligands. Indeed, the calculated energies of these states lower in the following the order: $\mathbf{1}_{O}$>$\mathbf{1}_{S}$>$\mathbf{1}_{Se}$>$\mathbf{1}_{Te}$. It is therefore possible that the S_1 or T_1 or both states of the chalcogen ligand fall too close or even below the emitting Dy^{3+}: $^4F_{9/2}$ state. In that case, lack of sensitization or efficient quenching of the lanthanide PL due to back energy transfer to the ligand would occur.

It should be pointed out that the observations based on the modelled Dy^{3+} ground state ($^6H_{15/2}$) are reliable, as confirmed by the good match between the *mj* levels retrieved from the *ab initio* calculations and the deconvolution of the $^4F_{9/2} \rightarrow {}^6H_{15/2}$ transition (**Figure S10**). However, modelling of the excited states is generally less accurate, and the absolute energy values of spin-orbit states are accompanied by a large error (**Figure S11**). This discrepancy also applies to the simulated thermometric performance of the complexes (**Figure 6d**). For this reason, particularly for the optical properties of the complexes, we analysed relative trends instead of absolute values. From these trends, a positive effect seems to be played by the introduction of soft chalcogen donors in the Dy^{3+} coordination sphere both in terms of magnetism and *mj*-level-based luminescence thermometry. Yet, the lowering of the ligand states' energy could frustrate these beneficial effects, up to a complete quenching of Dy^{3+} emission.

Conclusions

In conclusion, we reported the first thiobenzoate-based Ln^{3+}-SMM in the form of a mononuclear Dy^{3+} complex. Slow relaxation of the magnetization under no applied field was observed up to 12 K. The mechanisms involved in this process were interpreted combining analysis of magnetic data, photoluminescence spectrum and theoretical calculations. A ratiometric luminescence thermometry approach was established harnessing the thermal dependence of Dy^{3+} emission, with a relative thermal sensitivity between 0.6 and 1.1 $\%\cdot K^{-1}$ and temperature uncertainty <1 K across the 10-50 K temperature range. We subsequently used this complex as a model system to investigate how the introduction of different chalcogen donors (O, S, Se, Te) in the metal coordination sphere impact on the magnetic, optical, and luminescence thermometry performance. The trends obtained from *ab initio* calculations indicate that softer chalcogen donors can simultaneously boost the SMM performance and the sensitivity of thermometric approaches based on variations of the Stark levels' intensity. On the other hand, lowering of the energy states of the chalcogen-bearing ligand could result in an unfavourable energy scheme, and hence ultimately loss of appreciable Dy^{3+} emission.

Overall, this novel optomagnetic complex is a remarkable example of how the use of ligands that combine the features of soft (S, Se, and Te) and hard (O) donors (i.e., electronic cloud modulation and strong/weak interaction with the metal centre) is a promising strategy for the preparation of Ln^{3+}-SMMs with tailored optical properties. Moreover, the general considerations obtained from modelling of the family of complexes used herein as case study are envisaged to support the design of novel multifunctional Ln^{3+}-complexes based on soft-donor-bearing ligands that combine magnetic, optical, and luminescence thermometry properties.

Author Contributions

R.M. – Conceptualization, Data curation, Formal analysis, Funding acquisition, Investigation, Methodology, Visualization, Writing original draft

D.A.G. – Formal analysis, Investigation, Methodology, Writing original draft

R.G. – Formal analysis, Methodology, Writing original draft

J.O.M. – Formal analysis, Supervision, Methodology, Writing original draft

L.D.C. – Supervision, Writing – review & editing

D.J. – Supervision, Writing – review & editing

M.M. – Supervision, Writing – review & editing

Conflicts of interest

There are no conflicts to declare.

Acknowledgements

R.M. acknowledges the support of the European Commission through the European Union's Horizon 2020 research and innovation program under the Marie Skłodowska-Curie Grant agreement 797945 (LANTERNS). This work was supported by Ministerio de Ciencia e Innovación de España (PID2019-106211RB-I00) and developed within the scope of the project CICECO–Aveiro Institute of Materials, UIDB/50011/2020, financed by Portuguese funds through FCT/MEC and co-financed by FEDER under the PT2020 Partnership Agreement.

We thank the University of Ottawa, the CFI, and the NSERC for financial support of this work. J. O. M. and R. G. acknowledge Academy of Finland (project numbers 315829, 320015, and 345484) for funding. CSC-IT Centre for Science in Finland, the Finnish Grid and Cloud Infrastructure (persistent identifier urn:nbn:fi:research-infras-2016072533) and Prof. H. M. Tuononen (University of Jyväskylä) are acknowledged for providing computational resources for the project. We are greatly indebted to Dr. Josefina Perles Hernáez from the Interdepartmental Investigation Service (SIDI) of the Universidad Autónoma de Madrid for performing the X-ray diffraction experiment and solving the crystal structure of the complex investigated.

References and notes

* Due to the core-like nature of the 4f orbitals, it is expected that the lanthanides interact with the coordinating ligands through an electrostatic interaction rather than form a covalent bond. However, recent publications have shown that there can be a non-negligible covalent contribution to the bonding in the lanthanide complexes (Aravena et al., *Inorg. Chem.,* 2016, **55**, 4457-4469; Briganti et al., *Chem. Sci.*, 2019, **10**, 7233-7245; Panetti et al., *Nat. Commun.*, 2021, **12**, 1731). For the investigated systems, the AIM analyses support that the electrostatic interactions dominates the interaction between the coordinating ligands and Dy^{3+} ion, but this does not automatically rule out the plausible covalent contribution. Indeed, the values of $\nabla^2\rho(r)$ and DI for Ln-E bonds simultaneously decrease and increase, respectively, when descending the group 16. The results indicate that the covalent contribution of Ln-E bond gradually increases, when going from O to Te, albeit its ionic nature.

1. F. Arute, K. Arya, R. Babbush, D. Bacon, J. C. Bardin, R. Barends, R. Biswas, S. Boixo, F. Brandao, D. A. Buell, B. Burkett, Y. Chen, Z. Chen, B. Chiaro, R. Collins, W. Courtney, A. Dunsworth, E. Farhi, B. Foxen, A. Fowler, C. Gidney, M. Giustina, R. Graff, K. Guerin, S. Habegger, M. P. Harrigan, M. J. Hartmann, A. Ho, M. Hoffmann, T. Huang, T. S. Humble, S. V. Isakov, E. Jeffrey, Z. Jiang, D. Kafri, K. Kechedzhi, J. Kelly, P. V. Klimov, S. Knysh, A. Korotkov, F. Kostritsa, D. Landhuis, M. Lindmark, E. Lucero, D. Lyakh, S. Mandra, J. R. McClean, M. McEwen, A. Megrant, X. Mi, K. Michielsen, M. Mohseni, J. Mutus, O. Naaman, M. Neeley, C. Neill, M. Y. Niu, E. Ostby, A. Petukhov, J. C. Platt, C. Quintana, E. G. Rieffel, P. Roushan, N. C. Rubin, D. Sank, K. J. Satzinger, V. Smelyanskiy, K. J. Sung, M. D. Trevithick, A. Vainsencher, B. Villalonga, T. White, Z. J. Yao, P. Yeh, A. Zalcman, H. Neven and J. M. Martinis, *Nature*, 2019, **574**, 505-510.
2. D. N. Woodruff, R. E. Winpenny and R. A. Layfield, *Chem. Rev.*, 2013, **113**, 5110-5148.
3. J. Long, Y. Guari, R. A. S. Ferreira, L. D. Carlos and J. Larionova, *Coord. Chem. Rev.*, 2018, **363**, 57-70.
4. J. Long, J. Rouquette, J. M. Thibaud, R. A. Ferreira, L. D. Carlos, B. Donnadieu, V. Vieru, L. F. Chibotaru, L. Konczewicz, J. Haines, Y. Guari and J. Larionova, *Angew. Chem. Int. Ed. Engl.*, 2015, **54**, 2236-2240.
5. F. S. Guo, B. M. Day, Y. C. Chen, M. L. Tong, A. Mansikkamaki and R. A. Layfield, *Science*, 2018, **362**, 1400-1403.
6. D. Errulat, R. Marin, D. A. Galico, K. L. M. Harriman, A. Pialat, B. Gabidullin, F. Iikawa, O. D. D. Couto, Jr., J. O. Moilanen, E. Hemmer, F. A. Sigoli and M. Murugesu, *ACS. Cent. Sci.*, 2019, **5**, 1187-1198.
7. G. Brunet, R. Marin, M. J. Monk, U. Resch-Genger, D. A. Galico, F. A. Sigoli, E. A. Suturina, E. Hemmer and M. Murugesu, *Chem. Sci.*, 2019, **10**, 6799-6808.
8. D. A. Galico, R. Marin, G. Brunet, D. Errulat, E. Hemmer, F. A. Sigoli, J. O. Moilanen and M. Murugesu, *Chem. Eur. J.*, 2019, **25**, 14625-14637.
9. M. Fondo, J. Corredoira-Vázquez, A. M. García-Deibe, J. Sanmartín-Matalobos, M. Amoza, A. M. P. Botas, R. A. S. Ferreira, L. D. Carlos and E. Colacio, *Inorg. Chem. Frontiers*, 2020, **7**, 3019-3029.
10. R. A. S. Ferreira, E. Mamontova, A. M. P. Botas, M. Shestakov, J. Vanacken, V. Moshchalkov, Y. Guari, L. F. Chibotaru, D. Luneau, P. S. André, J. Larionova, J. Long and L. D. Carlos, *Adv. Opt. Mater.*, 2021, **9**, 2101495.
11. A. N. Carneiro Neto, E. Mamontova, A. M. P. Botas, C. D. S. Brites, R. A. S. Ferreira, J. Rouquette, Y. Guari, J. Larionova, J. Long and L. D. Carlos, *Adv. Opt. Mater.*, 2021, **10**, 2101870.
12. R. Marin, G. Brunet and M. Murugesu, *Angew. Chem. Int. Ed. Engl.*, 2021, **60**, 1728-1746.
13. F. Tuna, C. A. Smith, M. Bodensteiner, L. Ungur, L. F. Chibotaru, E. J. McInnes, R. E. Winpenny, D. Collison and R. A. Layfield, *Angew. Chem. Int. Ed. Engl.*, 2012, **51**, 6976-6980.
14. A. B. Canaj, S. Dey, O. Cespedes, C. Wilson, G. Rajaraman and M. Murrie, *Chem. Commun. (Camb.)*, 2020, **56**, 1533-1536.
15. G. A. Kumar, R. E. Riman and J. G. Brennan, *Coord. Chem. Rev.*, 2014, **273-274**, 111-124.
16. J. Xi, X. Ma, P. Cen, Y. Wu, Y. Q. Zhang, Y. Guo, J. Yang, L. Chen and X. Liu, *Dalton Trans.*, 2021, **50**, 2102-2111.
17. W. Huang, Z. Zheng and D. Wu, *Inorg. Chem. Commun.*, 2017, **84**, 40-44.
18. L. Tian and J. J. Vittal, *Cryst. Growth Des.*, 2006, **6**, 822-824.
19. T. Kanda, M. Ibi, K.-i. Mochizuki and S. Kato, *Chem. Lett.*, 1998, **27**, 957-958.
20. M. D. Regulacio, M. H. Pablico, J. A. Vasquez, P. N. Myers, S. Gentry, M. Prushan, S. W. Tam-Chang and S. L. Stoll, *Inorg. Chem.*, 2008, **47**, 1512-1523.
21. S.-S. Liu, J.-M. Zhao, S. Deng, J. Xiong, M.-F. Yang, J.-X. Li, S.-J. Lin, Y.-Q. Zhang and B.-W. Wang, *Inorg. Chem. Commun.*, 2018, **95**, 82-85.
22. D. Brown and D. G. Holah, *Chem. Commun. (London)*, 1968, **23**, 1545-1546.
23. J. H. Melman and T. J. Emge, *Chem. Commun.*, 1997, **23**, 2269-2270.
24. S. M. J. Aubin, Z. Sun, L. Pardi, J. Krzystek, K. Folting, L.-C. Brunel, A. L. Rheingold, G. Christou and D. N. Hendrickson, *Inorg. Chem.*, 1999, **38**, 5329-5340.
25. Y. Xin, J. Wang, M. Zychowicz, J. J. Zakrzewski, K. Nakabayashi, B. Sieklucka, S. Chorazy and S. I. Ohkoshi, *J. Am. Chem. Soc.*, 2019, **141**, 18211-18220.
26. S. A. Wade, S. F. Collins and G. W. Baxter, *J. Appl. Phys.*, 2003, **94**, 4743-4756.
27. C. D. S. Brites, A. Millán and L. D. Carlos, in Handbook on the Physics and Chemistry of Rare Earths, Vol. 49 (Eds: J.-C. G. Bünzli, V. K. Pecharsky) Elsevier Science, B. V. Amsterdam 2016, pp. 339-427.
28. A. Skripka, A. Morinvil, M. Matulionyte, T. Cheng and F. Vetrone, *Nanoscale*, 2019, **11**, 11322-11330.
29. L. Li, Y. Zhu, X. Zhou, C. D. S. Brites, D. Ananias, Z. Lin, F. A. A. Paz, J. Rocha, W. Huang and L. D. Carlos, *Adv. Funct. Mater.*, 2016, **26**, 8677-8684.

30. G. Bao, K. L. Wong, D. Jin and P. A. Tanner, *Light Sci. Appl.*, 2018, **7**, 96.
31. J. Wang, J. J. Zakrzewski, M. Zychowicz, V. Vieru, L. F. Chibotaru, K. Nakabayashi, S. Chorazy and S. I. Ohkoshi, *Chem. Sci.*, 2020, **12**, 730-741.
32. H. S. Wang, K. Zhang, J. Wang, Z. B. Hu, Z. Zhang, Y. Song and Y. Q. Zhang, *Inorg. Chem.*, 2021, **60**, 9941-9955.
33. K. R. Vignesh, D. I. Alexandropoulos, B. S. Dolinar and K. R. Dunbar, *Dalton Trans.*, 2019, **48**, 2872-2876.